

---

# SEDIMENT CONCENTRATION ESTIMATION VIA MULTISCALE INVERSE PROBLEM AND STOCHASTIC HOMOGENIZATION

---

A PREPRINT

Jiwei Li<sup>1</sup>, Lingyun Qiu<sup>2,3</sup>, Zhongjing Wang<sup>4,5</sup>, Hui Yu<sup>6</sup>, Siqin Zheng<sup>1</sup>

<sup>1</sup> Department of Mathematical Sciences, Tsinghua University, Beijing 100084, China  
(li-jw20@mails.tsinghua.edu.cn, zhengsq21@mails.tsinghua.edu.cn)

<sup>2</sup> Yau Mathematical Sciences Center, Tsinghua University, Beijing 100084, China

<sup>3</sup> Yanqi Lake Beijing Institute of Mathematical Sciences and Applications, Beijing 101408, China  
(lyqiu@tsinghua.edu.cn)

<sup>4</sup> Department of Hydraulic Engineering, Tsinghua University, Beijing 100084, China

<sup>5</sup> Breeding Base for State Key Laboratory of Land Degradation and Ecological Restoration in Northwest China, Ningxia University, Yinchuan 750021, Ningxia, China  
(zj.wang@tsinghua.edu.cn)

<sup>6</sup> School of Mathematics and Computational Science, Xiangtan University, Xiangtan 411105, Hunan, China  
(huiyu@xtu.edu.cn)

March 14, 2025

## ABSTRACT

In this work, we contribute to the broader understanding of inverse problems by introducing a versatile multiscale modeling framework tailored to the challenges of sediment concentration estimation. Specifically, we propose a novel approach for sediment concentration measurement in water flow, modeled as a multiscale inverse medium problem. To address the multiscale nature of the sediment distribution, we treat it as an inhomogeneous random field and use the homogenization theory in deriving the effective medium model. The inverse problem is formulated as the reconstruction of the effective medium model, specifically, the sediment concentration, from partial boundary measurements. Additionally, we develop numerical algorithms to improve the efficiency and accuracy of solving this inverse problem. Our numerical experiments demonstrate the effectiveness of the proposed model and methods in producing accurate sediment concentration estimates, offering new insights into sediment concentration measurement in complex environments.

**Keywords** sediment concentration measurement, multiscale modeling, inverse problem, homogenization theory

**MSC Classification** 35B27, 35R30, 76M50

## 1 Introduction

Sediment measurement stands as a cornerstone in environmental studies, hydraulic engineering, and geoscience research, as it provides crucial insights into the dynamics and characteristics of aquatic systems. Accurate quantification of sediment concentration in water bodies is essential for understanding sediment transport processes, assessing water quality, and designing effective erosion control measures. However, the inherent complexity of sediment dynamics coupled with limitations in measurement techniques poses significant challenges to achieving precise and reliable sediment concentration estimates.

Historically, sediment concentration measurement techniques have predominantly relied on direct sampling methods (see [19, 46, 42]) such as grab sampling, core sampling, and filtration. While these methods offer tangible measurements, they are often labor-intensive, time-consuming, and susceptible to spatial and temporal variability, limiting their applicability in dynamic environments. Moreover, these techniques may disrupt the natural sediment distribution and fail to capture fine-scale variations, leading to potential inaccuracies in concentration estimates.

In response to the shortcomings of direct sampling methods, researchers have explored a variety of indirect measurement approaches, including acoustic Doppler techniques [30, 11, 43, 44, 35, 13, 45], optical methods [40, 20, 3, 46], and remote sensing technologies [46, 33, 34, 9, 18]. This work contributes to the growing body of research on inverse problems by offering a multiscale modeling framework that addresses sediment concentration estimation with enhanced accuracy and efficiency. To achieve this, we propose a novel inverse problem formulation that integrates multiscale modeling and numerical optimization, providing robust and accurate estimates of sediment concentration even in complex environments.

Inverse problems involve estimating unknown parameters or properties of a system from observed data, often in situations where the relationship between the parameters and the observations is nonlinear, ill-posed, or underdetermined. In the context of sediment concentration measurement, the inverse problem entails determining the spatial distribution and temporal evolution of sediment concentration within a body of water from indirect measurements, such as remote acoustic data or optical signals. This problem is inherently challenging due to the complex and nonlinear relationship between sediment concentration and the observed data, as well as the multiscale nature of sediment distribution in aquatic environments.

Multiscale modeling effectively captures the complex and heterogeneous nature of physical systems, such as sediment concentration in water flow, which exhibits both fine-scale and large-scale variations. In [5, 6, 21], the authors apply the homogenization theory to derive the effective medium model for the propagation of seismic and elastic waves in the heterogeneous medium. Both the theoretical derivation and numerical results demonstrate the effectiveness of the homogenization theory in capturing the multiscale nature of wave propagation. However, these works, which are more focused on engineering applications, lack a rigorous mathematical proof for the homogenization process, limiting the theoretical foundation of the derived effective medium models. Additionally, their approaches are primarily designed for deterministic heterogeneous media, making them unsuitable for scenarios involving stochastic or random fields. We propose using stochastic homogenization theory to handle this multiscale nature for the following reasons:

1. At the microscopic scale, the positions of sediment particles vary rapidly, but the macroscopic distribution is relatively stable and crucial for understanding sediment concentration. Since the macroscopic distribution contains key properties of interest, such as sediment concentration, we focus on modeling the macroscopic sediment distribution, which is less sensitive to fine-scale fluctuations.
2. The microscopic variations make it challenging to model the detailed sediment structure. However, our primary focus is on the macroscopic sediment distribution, and homogenization theory provides an effective medium model that captures the macroscopic properties without needing to account for fine-scale details, offering a more efficient description of the system.
3. Using an effective medium model without fine-scale variations, we significantly reduce computational complexity. This simplification is vital for solving the inverse problem, which is often computationally expensive and requires numerous forward simulations.

The combination of inverse problem theory and multiscale modeling remains a relatively unexplored area due to the challenges in formulating and solving multiscale inverse problems. Direct simulation of such systems is impractical, and the nonlinear relationship between macroscopic properties and microscale observations further complicates the inverse problem. Recent advances in mathematical models and numerical methods have aimed to address these challenges. For example, [17] proposes general frameworks for solving multiscale inverse problems, including two-stage parameter estimation and direct estimation using the heterogeneous multiscale method (HMM, [12]). Nolen et al. propose various approaches to regularization of inverse problems, including Tikhonov and total variation regularization, and illustrate these ideas using a simple model for groundwater in [32]. In [31], the authors propose a strategy to quantify the slowly varying components of unknown coefficients by modeling their effect on the forward problem using the central limit theorem. This approach reduces Bayesian estimation to a weighted least-squares problem with a low-rank covariance matrix, independent of the number of measurements. Abdulle et al. [1] introduce a Bayesian approach combined with numerical homogenization to recover the macroscopic scalar parameters of the microscale tensor.

The paper is structured as follows. In Section 2, we provide a brief overview of several conventional instruments and associated technologies used to measure sediment concentration. Section 3 introduces the model for measuring sediment concentration in water flow. Section 4 outlines the numerical methods proposed to solve the multiscale inverse problem. Section 5 presents the numerical results that demonstrate the effectiveness of the model and methods. Finally, in Section 6, we summarize the key findings and conclude the paper.

## 2 Review of sediment concentration measurement methods

In this section, we provide a brief overview of several conventional instruments and associated technologies used to measure the sediment concentration. These methods include direct sampling[19, 46, 42], acoustic Doppler techniques[30, 11, 43, 44, 35, 13, 45], optical methods[40, 20, 3, 46], and remote sensing technologies[46, 33, 34, 9, 18]. In the following, we will discuss the principles, advantages, and limitations of each sort of methods, highlighting the challenges and opportunities in sediment concentration measurement.

Direct sampling methods are among the oldest and most commonly used techniques for measuring sediment concentration in water. These methods involve collecting sediment samples using tools such as sediment samplers, drying and weighing the sediment to calculate the volume concentration as  $m/(V\rho_s)$ , where  $m$  is the mass of sediment collected,  $V$  is the volume of sampled water and  $\rho_s$  is the density of sediment. While providing direct measurements, these methods are labor-intensive, time-consuming, and limited in spatial and temporal coverage. Moreover, their sensitivity is influenced by sampling and laboratory procedures [46, 40].

Acoustic Doppler meters, originally designed for flow-velocity measurements, can also estimate suspended sediment concentration by analyzing the intensity of backscattered sound waves. The relationship between backscatter intensity  $I$  and sediment concentration  $C$  is expressed as  $I = I_0 e^{-\alpha C}$ , where  $I_0$  is the intensity of incident sound, and  $\alpha$  is the attenuation coefficient determined through calibration (see details in [37, 23]). Researchers [13, 25, 39, 22] have also explored using signal-to-noise ratios from acoustic Doppler velocimeters to estimate sediment concentration. Also, the framework used to interpret the backscattered signals from suspensions of non-cohesive sediments can be found in [42]. While offering non-invasive, continuous measurements over large areas and depths, these techniques face challenges in translating backscatter data into sediment concentrations and may struggle to capture fine-scale variations.

Optical methods measure sediment concentration based on light attenuation, using sensors to detect light absorbed or scattered by suspended particles. Two common techniques, optical backscatter (OBS) and optical transmission, rely on infrared or visible light. OBS measures the backscattered light detected by photodiodes positioned around the emitter, with backscatter strength used to estimate the sediment concentration. Studies [20, 3] show a nearly linear response of OBS to homogeneous sediment concentrations over a wide range. Optical transmission measures light attenuation as it passes through the sample, offering higher sensitivity to low particle concentrations. However, both methods are affected by the particle size according to [3, 47, 29, 10].

Remote sensing technologies, including satellite and aerial imagery, estimate sediment concentration in large water bodies based on spectral reflectance, where reflected light is related to water properties like suspended particle concentration. Studies [34, 33, 2, 9] have explored the correlation between sediment concentration and reflected radiation. While these methods provide spatially continuous measurements over large areas, they may struggle to capture small variations in sediment concentration. Additionally, large errors can occur when the sediment type is unknown due to the strong correlation between spectral readings and sediment mineral composition stated in [33, 9].

## 3 Mathematical model

In this section, we present the model for the measurement of sediment concentration in the water flow. We will first introduce the physical model governing the acoustic wave propagation in sediment-laden water flow. Then we will present the stochastic homogenization theory to derive the effective medium model associated with the heterogeneous model. Finally, we will formulate the multiscale inverse problem to estimate the sediment concentration from the measurements of the wave field on the boundary.

Similar to the acoustic Doppler techniques, we consider the measurement environment as the water flow with sediment concentration and arrange the transmitters and receivers on the boundary of the measurement domain. The acoustic wave field is emitted by the transmitters, propagates in the heterogeneous medium, and is measured by the receivers. However, what our model differs from the acoustic Doppler techniques is that we will study how the wave field propagates in the heterogeneous medium more deeply and propose the multiscale inverse problem to estimate the sediment concentration, rather than directly calibrating the relationship between the decrease of the amplitude of the acoustic wave and the sediment concentration.

### 3.1 Acoustic structure of sediment-laden flow

Firstly, we introduce a physical model to describe the sediment concentration in water flow using the p-wave velocity. Drawing inspiration from acoustic Doppler-based instruments and the distinct acoustic properties of sediment and water, we model the sediment distribution as a highly heterogeneous acoustic medium, denoted by  $c_\epsilon(x, t)$ . This

function represents the p-wave velocity, which varies depending on the medium: at a given location  $x$  and time  $t$ ,  $c_\epsilon(x, t)$  corresponds to the p-wave velocity in sediment if sediment is present; otherwise, it reflects the p-wave velocity in water.

Next, consider the sediment distribution in a river as an example. At the macroscopic scale, sediment particles are primarily concentrated near the riverbed, with the concentration gradually decreasing as the depth decreases. At the microscopic scale, however, individual sediment particles are distributed randomly and exhibit rapid variations. This variability highlights the nature of the p-wave velocity  $c_\epsilon(x, t)$ , which reflects the heterogeneous distribution of sediment as a multiscale field.

To describe this multiscale behavior, we introduce a smooth function  $p(x, t)$  to represent the probability of sediment present at location  $x$  and time  $t$ . The instantaneous sediment concentration can then be expressed as the integral of  $p(x, t)$  with respect to  $x$ . Notably, the propagation speed of the p-wave is much faster than the sediment transport speed, allowing us to approximate the sediment distribution as a static field during wave propagation. Thus, we have  $p(x, t) \approx p(x)$  and  $c_\epsilon(x, t) \approx c_\epsilon(x)$ .

More formally, the heterogeneous p-wave velocity is modeled as the Poisson cloud model. It is based on a heterogeneous Poisson point process, a widely used random process that describes the random distribution of particles in the space [27].

**Definition 1.** A Poisson point process on  $\mathbb{R}^d$  with a heterogeneity scale  $\epsilon > 0$  and a nonnegative density function  $\rho$  is a random countable subset  $\Pi_\epsilon$  of  $\mathbb{R}^d$ , satisfying that

1. for any Borel subset  $A$  of  $\mathbb{R}^d$ , the number of points in  $\Pi_\epsilon \cap A$ , denoted by  $N_\epsilon(A)$ , is a random variable following the Poisson law with mean

$$\lambda_\epsilon(A) = \frac{1}{V_d \epsilon^d} \int_A \rho(x) dx,$$

where  $V_d$  is the volume of the unit ball in  $\mathbb{R}^d$ , and

2. for any disjoint Borel subsets  $A_1, \dots, A_k$  of  $\mathbb{R}^d$ , the random variables  $N_\epsilon(A_1), \dots, N_\epsilon(A_k)$  are independent.

The parameter  $\epsilon$  is the characteristic length scale, which represents the size of the small-scale sediments. Intuitively, the smaller the sediment size  $\epsilon$ , the more sediments are in the same set  $A$  on average, so it is reasonable in the definition to divide the density function  $\rho$  by the volume of a ball with radius  $\epsilon$ .

Viewing the sediments as spherical particles of radius  $\epsilon$ , denoted by  $B(x, \epsilon)$  with  $x$  representing their locations, we define the random field of the heterogeneous p-wave velocity over the space as

$$c_\epsilon(x) = c_\epsilon(x, \Pi_\epsilon) = \begin{cases} c_1, & \text{dist}(x, \Pi_\epsilon) < \epsilon, \\ c_0, & \text{dist}(x, \Pi_\epsilon) \geq \epsilon, \end{cases} \quad (3.1)$$

where  $c_0$  and  $c_1$  denote the p-wave velocity of water and sediments respectively, which are assumed to be constant for simplicity. Therefore, the probability of sediments arising at location  $x \in \mathbb{R}^d$  is

$$p_\epsilon(x) = 1 - \mathbb{P}[N_\epsilon(B(x, \epsilon)) = 0] = 1 - e^{-\int_{B(x, \epsilon)} \rho(y) dy}. \quad (3.2)$$

Since  $\int_{B(x, \epsilon)} \rho(y) dy \rightarrow \rho(x)$  as  $\epsilon \rightarrow 0$  for continuous  $\rho$ , it is natural to define

$$p(x) = \lim_{\epsilon \rightarrow 0} p_\epsilon(x) = 1 - e^{-\rho(x)} \quad (3.3)$$

as the probability of sediments arising at location  $x \in \mathbb{R}^d$  at the macroscopic scale.

### 3.2 Wave propagation in heterogeneous medium

Consider the highly heterogeneous velocity profile  $c_\epsilon(x)$  representing the p-wave velocity at  $x$  in the flow. For simplicity, we assume that the velocity profile  $c_\epsilon$  varies rapidly in a bounded domain  $D \subset \mathbb{R}^d$  ( $d = 2, 3$ ) and is constant outside  $D$ . It means that the density function  $\rho(x)$  defined in the Poisson cloud model vanishes outside  $D$ , i.e.  $\text{supp } \rho \subset \bar{D}$ . Given a known acoustic source  $f(x, t)$ , the equation governing the wave propagation is given by the following wave equation:

$$\left( \frac{1}{c_\epsilon^2(x)} \partial_t^2 - \Delta \right) u_\epsilon = f, \quad x \in \mathbb{R}^d, t \in (0, T), \quad (3.4a)$$

$$u_\epsilon(x, 0) = 0, \quad x \in \mathbb{R}^d, \quad (3.4b)$$

$$\partial_t u_\epsilon(x, 0) = 0, \quad x \in \mathbb{R}^d. \quad (3.4c)$$

Let the slowness square  $m_\epsilon(x)$  be  $1/c_\epsilon^2(x)$ . The solution  $u_\epsilon(x, t)$  of (3.4) represents the wave field propagating in the heterogeneous medium. It is measured by the receivers located at the partial boundary  $\Gamma \subset \partial D$ , and the measurements  $u_\epsilon|_{\Gamma \times (0, T)}$  are used to infer the sediment distribution  $p(x)$ . For convenience, we rewrite the measurement of the wave field as an operator

$$\mathcal{G}_{\text{het}}^\epsilon : m_\epsilon(x) \mapsto u_\epsilon|_{\Gamma \times (0, T)}. \quad (3.5)$$

However, the highly heterogeneous nature of the p-wave velocity  $c_\epsilon(x)$  makes the direct solution of (3.4) computationally expensive, which means that a quite fine mesh is required to capture the small-scale heterogeneity. Moreover, we are interested in the macroscopic sediment distribution  $p(x)$  instead of any concrete microscopic structure of  $c_\epsilon(x)$ . To avoid recovering specific realizations of  $c_\epsilon(x)$ , we consider the stochastic homogenization theory to derive the effective medium model, where the effective coefficient directly matches the sediment distribution  $p(x)$ . In the following, we will present the stochastic homogenization theory based on the wave equation (3.4) in the frequency domain, i.e. the Helmholtz equation.

### 3.3 Stochastic homogenization of wave equations

Suppose that the acoustic source  $f$  is in the form of

$$f(x, t) = \int_I f_\omega(x) e^{i\omega t} d\omega$$

with a bounded interval  $I \subset \mathbb{R}_+$ . This assumption is quite practical, since the acoustic source we use in practice always has a finite frequency band. By linearity, the solution to the wave equation (3.4) can be decomposed as

$$u_\epsilon(x, t) = \int_I u_{\epsilon, \omega}(x) e^{i\omega t} d\omega,$$

with the components  $u_{\epsilon, \omega}$  solving the Helmholtz equation

$$(-\omega^2 m_\epsilon(x) - \Delta) u_{\epsilon, \omega} = f_\omega, \quad x \in \mathbb{R}^d. \quad (3.6)$$

For simplicity in the following analysis, we generalize the coefficients of (3.6) to the complex domain, omit the subscript  $\omega$  and rewrite it as

$$-(\Delta + k^2 \underline{n}_\epsilon^2(x)) u_\epsilon = f, \quad x \in \mathbb{R}^d, \quad (3.7)$$

where  $k = \omega/c_0$  is the wave number with frequency  $\omega$  in water, and  $\underline{n}_\epsilon^2(x)$  is the complex refractive index, which equals  $\underline{n}_0^2 = 1 + i\kappa_0$  in water and  $\underline{n}_1^2 = n_1^2 + i\kappa_1$  in sand. Here  $n_1 = c_0/c_1$  denotes the real refractive index between water and sand, and we add the absorption  $\kappa_0, \kappa_1 > 0$  in water and sand, to bypass the analysis involving the radiation condition at infinity. As a result, any source  $f \in L^2(\mathbb{R}^d)$  immediately gives rise to a unique solution to (3.7) in  $L^2(\mathbb{R}^d)$ . For the sake of simplicity, we have omitted the subscript  $\omega$  and follow the same notation  $u_\epsilon$  and  $f$  in (3.4), which would not lead to any confusion since  $u_\epsilon$  and  $f$  only depend on  $x$  in the analysis of Section 3.3 and Section 3.4.

In the next subsection, we will proceed as in [26] to derive the effective model of (3.7), with the random coefficient field

$$\underline{n}_\epsilon^2(x) = \underline{n}_\epsilon^2(x, \Pi_\epsilon) = \begin{cases} \underline{n}_1^2, & \text{dist}(x, \Pi_\epsilon) < \epsilon, \\ \underline{n}_0^2, & \text{dist}(x, \Pi_\epsilon) \geq \epsilon. \end{cases}$$

modeled by the Poisson cloud defined in Definition 1. The rigorous statement is provided as follows:

**Theorem 1.** *If  $\rho \in C^\alpha(\mathbb{R}^d)$  for some  $\alpha \in (0, 1]$  with the  $\alpha$ -Hölder seminorm*

$$[\rho]_\alpha = \sup_{x \neq y} \frac{|\rho(x) - \rho(y)|}{|x - y|^\alpha}$$

and support  $\bar{D}$ , then the homogenized equation of (3.7) is

$$-(\Delta + k^2 \mu(x)) u = f, \quad x \in \mathbb{R}^d, \quad (3.8)$$

where

$$\mu(x) = \lim_{\epsilon \rightarrow 0} \mathbb{E}[\underline{n}_\epsilon^2] = p(x) \underline{n}_1^2 + (1 - p(x)) \underline{n}_0^2. \quad (3.9)$$

Moreover, there exists a constant  $C$ , depending on  $k, \underline{n}_0^2, \underline{n}_1^2, d, \alpha, [\rho]_\alpha, |D|$ , such that

$$\mathbb{E} \|u_\epsilon - u\|_{L^2(\mathbb{R}^d)}^2 \leq C \epsilon^{2\alpha} \|u\|_{L^2(\mathbb{R}^d)}^2. \quad (3.10)$$

According to Theorem 1, we can claim that the effective model corresponding to (3.6) is

$$(-\omega^2 m(x) - \Delta) u_\omega = f_\omega, \quad x \in \mathbb{R}^d, \quad (3.11)$$

where

$$m(x) = \lim_{\epsilon \rightarrow 0} \mathbb{E}[m_\epsilon(x)] = \frac{p(x)}{c_1^2} + \frac{1-p(x)}{c_0^2} \quad (3.12)$$

is the effective slowness. Noting the boundedness of  $I$ , the integral

$$u(x, t) = \int_I u_\omega(x) e^{i\omega t} d\omega$$

is the effective wave field of the heterogeneous wave equation (3.4), satisfying the equation

$$(m(x)\partial_t^2 - \Delta) u = f, \quad x \in \mathbb{R}^d, t \in (0, T), \quad (3.13a)$$

$$u(x, 0) = 0, \quad x \in \mathbb{R}^d, \quad (3.13b)$$

$$\partial_t u(x, 0) = 0, \quad x \in \mathbb{R}^d, \quad (3.13c)$$

which is the effective model we aim to derive.

Denote the effective velocity as  $c(x) = 1/\sqrt{m(x)}$ . Note that the effective medium  $m(x)$  is defined on the macroscopic scale, and it captures the average behavior of the heterogeneous medium  $m_\epsilon(x)$ . Hence, it is more computationally efficient to solve (3.13) than to solve (3.4). According to Theorem 1, the solution  $u(x, t)$  of (3.13) is believed to be a good approximation of the solution  $u_\epsilon(x, t)$  of (3.4) in the sense of expectation. We also rewrite the effective model as an operator:

$$\mathcal{G}_{\text{eff}} : m(x) \mapsto u|_{\Gamma \times (0, T)}. \quad (3.14)$$

To verify the effectiveness of the effective model (3.13), we design numerical experiments in Section 5. More precisely, we generate the heterogeneous medium and the effective medium in the discrete domain  $D$  and compare the wave field propagation in each medium. We expect the effective wave field to closely match the heterogeneous wave field. Indeed, the results will demonstrate the effectiveness of the homogenization theory in capturing the multiscale nature of wave propagation, providing strong evidence that  $u(x, t)$  represents the average of  $u_\epsilon(x, t)$ .

### 3.4 Proof of Theorem 1

For ease of notations, we shall abbreviate the function space  $L^2(\mathbb{R}^d)$  with  $L^2$ , and use  $C(\cdot)$  to denote the constant with dependence in parentheses. The complex conjugate of a complex number  $z$  is denoted by  $z^*$ . Before proving Theorem 1, we prepare with two lemmas.

**Lemma 1.** *Let  $g \in L^2$  and  $v$  solve*

$$-(\Delta + k^2 q(x)) v = g \text{ in } \mathbb{R}^d. \quad (3.15)$$

*If*

$$\inf_{x \in \mathbb{R}^d} \text{Im } q(x) = c > 0,$$

*then*

$$\|v\|_{L^2} \leq k^{-2} c^{-1} \|g\|_{L^2}. \quad (3.16)$$

*Proof.* Multiplying (3.15) by  $v^*$ , integrating by parts over  $\mathbb{R}^d$  and taking the imaginary part lead to

$$k^2 c \|v\|_{L^2}^2 \leq k^2 \int_{\mathbb{R}^d} \text{Im } q(x) |v(x)|^2 dx = -\text{Im} \int_{\mathbb{R}^d} g(x) v^*(x) dx \leq \|g\|_{L^2} \|v\|_{L^2},$$

and (3.16) follows.  $\square$

One of the applications of this lemma is to derive an estimate for the Green function of the homogenized equation (3.8).

**Lemma 2.** *For any  $y \in \mathbb{R}^d$ , let  $G(\cdot, y)$  be the solution to*

$$-(\Delta + k^2 \mu) G(\cdot, y) = \delta_y \text{ in } \mathbb{R}^d$$

*with  $\mu$  defined by (3.9). Then there exists a constant  $C$  depending on  $k, \underline{n}_0^2, \underline{n}_1^2, d$  such that*

$$\sup_{y \in \mathbb{R}^d} \|G(\cdot, y)\|_{L^2}^2 \leq C.$$

*Proof.* We firstly derive an estimate for the Green function  $G_0$  of the operator  $-(\Delta + k^2 \underline{n}_0^2)$  with constant coefficient. Since  $\text{Im } \underline{n}_0^2 = \kappa_0 > 0$ , we define  $\underline{n}_0$  to be the principal square root of  $\underline{n}_0^2$  (i.e. the evaluation of the single-valued branch of  $\sqrt{\cdot}$  on  $\mathbb{C} \setminus \mathbb{R}_+$ ), so that  $\text{Im } \underline{n}_0 > 0$ . Then the Green function admits the following explicit formulas:

$$G_0(x, y) = \begin{cases} \frac{e^{ik\underline{n}_0|x-y|}}{4\pi|x-y|}, & d = 3, \\ \frac{i}{4} H_0^{(1)}(k\underline{n}_0|x-y|), & d = 2, \end{cases}$$

where  $H_0^{(1)}$  is the zeroth order Hankel function of the first kind.

For  $d = 3$  and any  $y \in \mathbb{R}^3$ , by direct calculation we have

$$\begin{aligned} \|G_0(\cdot, y)\|_{L^2}^2 &= \int_{\mathbb{R}^3} |G_0(x, y)|^2 dx \\ &= \frac{1}{(4\pi)^2} \int_{\mathbb{R}^3} \frac{e^{-2k|x-y|\text{Im } \underline{n}_0}}{|x-y|^2} dx \\ &= \frac{1}{4\pi} \int_0^\infty e^{-2kr \text{Im } \underline{n}_0} dr = \frac{1}{8\pi k \text{Im } \underline{n}_0}. \end{aligned}$$

For  $d = 2$ , since the Hankel function  $H_0^{(1)}$  has no analytic expressions, we need to involve its asymptotic behavior at infinity

$$H_0^{(1)}(z) \sim \sqrt{\frac{2}{\pi z}} e^{i(z - \frac{\pi}{4})}, \quad \arg z \in (-\pi, 2\pi), \quad |z| \rightarrow \infty.$$

Since

$$\begin{aligned} \int_{\mathbb{R}^2} \left| \sqrt{\frac{2}{\pi k \underline{n}_0 |x-y|}} e^{i(k\underline{n}_0|x-y| - \frac{\pi}{4})} \right|^2 dx &= \int_{\mathbb{R}^2} \frac{2}{\pi k |\underline{n}_0| |x-y|} e^{-2k|x-y|\text{Im } \underline{n}_0} dx \\ &= \frac{2}{\pi k |\underline{n}_0|} \int_0^\infty e^{-2kr \text{Im } \underline{n}_0} dr = \frac{1}{\pi k^2 |\underline{n}_0| \text{Im } \underline{n}_0}, \end{aligned}$$

we obtain that

$$\sup_{y \in \mathbb{R}^d} \|G_0(\cdot, y)\|_{L^2}^2 \leq C(k, \underline{n}_0).$$

Now we turn to prove the estimate of  $G$ . For any  $y \in \mathbb{R}^d$ , since

$$-(\Delta + k^2 \mu)(G(\cdot, y) - G_0(\cdot, y)) = k^2 (\underline{n}_1^2 - \underline{n}_0^2) p G_0(\cdot, y) \text{ in } \mathbb{R}^d$$

and

$$\inf_{x \in \mathbb{R}^d} \text{Im } \mu(x) = \inf_{x \in \mathbb{R}^d} \{p(x)\kappa_1 + (1-p(x))\kappa_0\} \geq \min\{\kappa_0, \kappa_1\} =: \kappa_m > 0,$$

applying Lemma 1 we derive

$$\begin{aligned} \|G(\cdot, y) - G_0(\cdot, y)\|_{L^2} &\leq k^{-2} \kappa_m^{-1} \|k^2 (\underline{n}_1^2 - \underline{n}_0^2) p G_0(\cdot, y)\|_{L^2} \\ &\leq \kappa_m^{-1} |\underline{n}_1^2 - \underline{n}_0^2| \|G_0(\cdot, y)\|_{L^2}. \end{aligned}$$

It follows that

$$\|G(\cdot, y)\|_{L^2}^2 \leq (1 + \kappa_m^{-1} |\underline{n}_1^2 - \underline{n}_0^2|)^2 \|G_0(\cdot, y)\|_{L^2}^2 \leq C(k, \underline{n}_0^2, \underline{n}_1^2, d).$$

□

*Proof of Theorem 1.* By (3.7) and (3.8) we have

$$-(\Delta + k^2 \mu)(u_\epsilon - u) = k^2 (\underline{n}_\epsilon^2 - \mu) u_\epsilon \text{ in } \mathbb{R}^d.$$

Denoting the solution operator of the homogenized equation (3.8) by  $\mathcal{G}$ , which is the convolution operator with kernel  $G$ , we have

$$u_\epsilon - u = k^2 \mathcal{G} r_\epsilon u_\epsilon = k^2 \mathcal{G} r_\epsilon u + k^2 \mathcal{G} r_\epsilon (u_\epsilon - u),$$

where  $r_\epsilon(x) = \underline{n}_\epsilon^2(x) - \mu(x)$  takes the value of  $(1 - p(x))(\underline{n}_1^2 - \underline{n}_0^2)$  with probability  $p_\epsilon(x)$  and  $-p(x)(\underline{n}_1^2 - \underline{n}_0^2)$  with probability  $1 - p_\epsilon(x)$ . Define  $v_\epsilon = k^2 \mathcal{G} r_\epsilon u$ , solving the equation

$$-(\Delta + k^2 \mu(x))v_\epsilon = k^2 r_\epsilon u \text{ in } \mathbb{R}^d. \quad (3.17)$$

Then we need to estimate  $v_\epsilon$  and  $u_\epsilon - u - v_\epsilon$ . For the latter, by (3.7), (3.8) and (3.17) we derive

$$-(\Delta + k^2 \underline{n}_\epsilon^2(x))(u_\epsilon - u - v_\epsilon) = k^2 r_\epsilon v_\epsilon \text{ in } \mathbb{R}^d.$$

Since  $\text{Im } \underline{n}_\epsilon^2(x) \geq \kappa_m$  for all  $x \in \mathbb{R}^d$ , Lemma 1 shows that

$$\begin{aligned} \|u_\epsilon - u - v_\epsilon\|_{L^2} &\leq k^{-2} \kappa_m^{-1} \|k^2 r_\epsilon v_\epsilon\|_{L^2} \\ &\leq \kappa_m^{-1} \|r_\epsilon\|_{L^\infty} \|v_\epsilon\|_{L^2} \leq \kappa_m^{-1} |\underline{n}_1^2 - \underline{n}_0^2| \|v_\epsilon\|_{L^2}. \end{aligned}$$

So

$$\|u_\epsilon - u\|_{L^2} \leq (1 + \kappa_m^{-1} |\underline{n}_1^2 - \underline{n}_0^2|) \|v_\epsilon\|_{L^2}. \quad (3.18)$$

Employing the Green function representation of  $v_\epsilon$ , we have

$$\begin{aligned} \|v_\epsilon\|_{L^2}^2 &= \int_{\mathbb{R}^d} v_\epsilon(x) v_\epsilon^*(x) dx \\ &= k^4 \int_{\mathbb{R}^d} \int_{\mathbb{R}^d} G(x, y) r_\epsilon(y) u(y) dy \int_{\mathbb{R}^d} G^*(x, z) r_\epsilon^*(z) u^*(z) dz dx, \end{aligned}$$

and it follows that

$$\begin{aligned} \mathbb{E} \|v_\epsilon\|_{L^2}^2 &= k^4 \int_{\mathbb{R}^d} \int_{\mathbb{R}^d \times \mathbb{R}^d} G(x, y) G^*(x, z) \mathbb{E}[r_\epsilon(y) r_\epsilon^*(z)] u(y) u^*(z) dy dz dx \\ &= k^4 \int_{\mathbb{R}^d \times \mathbb{R}^d} \left( \int_{\mathbb{R}^d} G(x, y) G^*(x, z) dx \right) \mathbb{E}[r_\epsilon(y) r_\epsilon^*(z)] u(y) u^*(z) dy dz \\ &\leq C(k, \underline{n}_0^2, \underline{n}_1^2, d) \int_{\mathbb{R}^d \times \mathbb{R}^d} |\mathbb{E}[r_\epsilon(y) r_\epsilon^*(z)]| |u(y)| |u(z)| dy dz. \end{aligned}$$

We split the integral on the right into two parts,

$$\begin{aligned} I_1 &= \int_{\{|y-z| \geq 2\epsilon\}} |\mathbb{E}[r_\epsilon(y) r_\epsilon^*(z)]| |u(y)| |u(z)| dy dz, \\ I_2 &= \int_{\{|y-z| < 2\epsilon\}} |\mathbb{E}[r_\epsilon(y) r_\epsilon^*(z)]| |u(y)| |u(z)| dy dz, \end{aligned}$$

and estimate them separately. For the first part, we make use of the independence assumption of the Poisson point process. When  $|y - z| \geq 2\epsilon$ , we have  $B(y, \epsilon) \cap B(z, \epsilon) = \emptyset$ , so the random variables  $N_\epsilon(B(y, \epsilon))$  and  $N_\epsilon(B(z, \epsilon))$  are independent, and so are  $r_\epsilon(y)$  and  $r_\epsilon(z)$  being their function respectively. Hence,

$$\mathbb{E}[r_\epsilon(y) r_\epsilon^*(z)] = \mathbb{E}[r_\epsilon(y)] \mathbb{E}[r_\epsilon^*(z)]^* = |\underline{n}_1^2 - \underline{n}_0^2|^2 (p_\epsilon(y) - p(y))(p_\epsilon(z) - p(z)),$$

and

$$\begin{aligned} I_1 &= |\underline{n}_1^2 - \underline{n}_0^2|^2 \int_{\{|y-z| \geq 2\epsilon\}} |p_\epsilon(y) - p(y)| |p_\epsilon(z) - p(z)| |u(y)| |u(z)| dy dz \\ &\leq |\underline{n}_1^2 - \underline{n}_0^2|^2 \left( \int_{\mathbb{R}^d} |p_\epsilon(y) - p(y)| |u(y)| dy \right)^2 \leq |\underline{n}_1^2 - \underline{n}_0^2|^2 \|p_\epsilon - p\|_{L^2}^2 \|u\|_{L^2}^2. \end{aligned}$$

Since  $\rho$  is nonnegative and  $C^\alpha$  with support  $\bar{D}$ , we have

$$\begin{aligned} |p_\epsilon(x) - p(x)| &= \left| e^{-\int_{B(x, \epsilon)} \rho(y) dy} - e^{-\rho(x)} \right| \\ &\leq \left| \int_{B(x, \epsilon)} \rho(y) dy - \rho(x) \right| \\ &\leq \int_{B(x, \epsilon)} |\rho(y) - \rho(x)| dy \leq C(d, \alpha, [\rho]_\alpha) \epsilon^\alpha. \end{aligned}$$



Then

$$I_1 \leq C(\underline{n}_0^2, \underline{n}_1^2, d, \alpha, [\rho]_\alpha, |D|) \epsilon^{2\alpha} \|u\|_{L^2}^2. \quad (3.19)$$

As for the second part, we have

$$\begin{aligned} I_2 &\leq |\underline{n}_1^2 - \underline{n}_0^2|^2 \int_{\{|y-z| < 2\epsilon\}} |u(y)| |u(z)| \, dy \, dz \\ &= |\underline{n}_1^2 - \underline{n}_0^2|^2 \int_{\mathbb{R}^d} |u(y)| \int_{B(y, 2\epsilon)} |u(z)| \, dz \, dy. \end{aligned}$$

Denoting

$$\mathcal{M}u(y) = \sup_{r>0} \int_{B(y,r)} |u(z)| \, dz$$

as the Hardy-Littlewood maximal function of  $u$ , we further have

$$I_2 \leq |\underline{n}_1^2 - \underline{n}_0^2|^2 V_d(2\epsilon)^d \int_{\mathbb{R}^d} |u(y)| |\mathcal{M}u(y)| \, dy \leq C(\underline{n}_0^2, \underline{n}_1^2, d) \epsilon^d \|u\|_{L^2} \|\mathcal{M}u\|_{L^2}.$$

Incorporated with the maximal function theorem [24, Theorem 2.2]

$$\|\mathcal{M}u\|_{L^2} \leq C(d) \|u\|_{L^2},$$

it follows that

$$I_2 \leq C(\underline{n}_0^2, \underline{n}_1^2, d) \epsilon^d \|u\|_{L^2}^2. \quad (3.20)$$

Since  $2\alpha \leq 2 \leq d$ , combining (3.19) and (3.20) yields that

$$\mathbb{E}\|v_\epsilon\|_{L^2}^2 \leq C(k, \underline{n}_0^2, \underline{n}_1^2, d)(I_1 + I_2) \leq C(k, \underline{n}_0^2, \underline{n}_1^2, d, \alpha, [\rho]_\alpha, |D|) \epsilon^{2\alpha} \|u\|_{L^2}^2.$$

Finally, by (3.18) we conclude that

$$\mathbb{E}\|u_\epsilon - u\|_{L^2}^2 \leq (1 + \kappa_m^{-1} |\underline{n}_1^2 - \underline{n}_0^2|)^2 \mathbb{E}\|v_\epsilon\|_{L^2}^2 \leq C(k, \underline{n}_0^2, \underline{n}_1^2, d, \alpha, [\rho]_\alpha, |D|) \epsilon^{2\alpha} \|u\|_{L^2}^2. \quad \square$$

### 3.5 Multiscale inverse problem

In the following, we denote the data generated by the heterogeneous medium as  $d_{\text{het}}$  and the data generated by the effective medium as  $d_{\text{eff}}$ . Due to the expensive computational cost of the direct inversion of the operator  $\mathcal{G}_{\text{het}}^\epsilon$ , many frameworks have been proposed to solve the inverse problems associated with the multiscale nature. Inspired by the study in [17] and considering the explicit form of the homogenized equation, we propose the following multiscale inverse problem formulation:

$$\min_{m(x)} \text{dist}(\mathcal{G}_{\text{eff}}(m), d_{\text{het}}), \quad (3.21)$$

which replaces the synthetic data  $d_{\text{eff}}$  with the real measurements  $d_{\text{het}}$ . Here the distance function  $\text{dist}(\cdot, \cdot)$  is a suitable metric to measure the discrepancy between the synthetic data and the real measurements.

The formulation (3.21) bears a strong resemblance to the full waveform inversion (FWI, [28, 41]) problem in seismology, which seeks to reconstruct the subsurface model using seismic data. However, there is a fundamental difference between the two. In FWI, the observed data is typically assumed to lie within the range of the forward operator, disregarding the effects of noise or model imperfections. In contrast, the data  $d_{\text{het}}$  in our problem exhibits multiscale and high-frequency characteristics, introducing complexities that prevent it from being contained within the range of  $\mathcal{G}_{\text{eff}}$ . To address these complexities, we summarize the key challenges of solving this multiscale inverse problem as follows:

1. The operator  $\mathcal{G}_{\text{eff}}$  is nonlinear, which makes the inverse problem ill-posed and difficult to solve numerically.
2. The data  $d_{\text{het}}$  has a multiscale, stochastic and high-frequency nature, which makes the inverse problem underdetermined.

To address these challenges, we propose the following numerical strategies to enhance the performance of the multiscale inverse problem, with their details discussed in Remark 1.

1. The use of regularization techniques to stabilize the inverse problem and prevent overfitting.

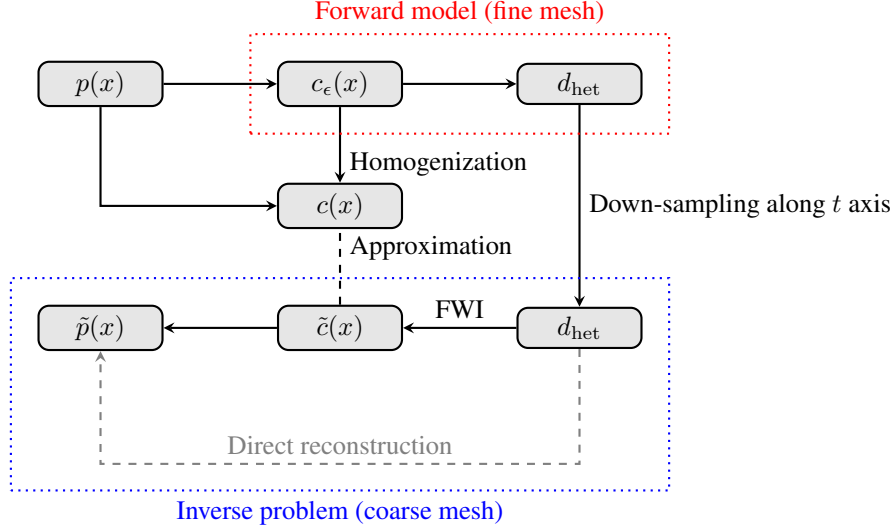


Figure 1: The diagram of numerical simulations.

2. Representations of the effective medium model  $m(x)$  in terms of a reduced basis or a sparse representation to reduce the dimensionality of the problem and improve computational efficiency.
3. Combination of multiple measurement data to diminish the impact of the multiscale nature of the data and enhance the robustness of the solution.

In the following section, we will present the numerical methods according to the proposed strategies in detail and demonstrate their effectiveness in solving the multiscale inverse problem.

## 4 Numerical approach

The overall workflow of the numerical simulations is illustrated in Figure 1. Broadly, the process consists of two components: forward modeling (fine mesh) and solving the inverse problem (coarse mesh). The forward modeling involves generating synthetic data  $d_{\text{het}}$  based on the heterogeneous medium  $c_\epsilon(x)$ , while the inverse problem focuses on recovering the effective medium  $c(x)$  and the sediment distribution  $p(x)$  from the measurements  $d_{\text{het}}$ . It is important to note that the synthetic data  $d_{\text{het}}$  in forward modeling is generated on a fine mesh to mimic real measurements and capture the multiscale characteristics of the data. In contrast, all simulations for the inverse problem are carried out on a coarse mesh. Once we get the heterogeneous data  $d_{\text{het}}$ , we will first preprocess these data to obtain the data suitable for inversion, and then solve the inverse problem to get  $\tilde{c}(x)$  and  $\tilde{p}(x)$ . According to Theorem 1, the recovered effective medium  $\tilde{c}(x)$  is expected to closely match the true effective medium  $c(x)$  corresponding to the heterogeneous medium  $c_\epsilon(x)$ . Besides, one could directly reconstruct the sediment distribution  $\tilde{p}(x)$  from the data  $d_{\text{het}}$  skipping the medium recovery step. In the following, we will introduce the numerical methods for each step of the diagram in detail.

### 4.1 Closed form of effective models

For the physical modeling of the sediment distribution in Section 3.1, we have derived the effective medium model  $m(x)$  according to (3.12), which is

$$m(x) = \frac{1}{c^2(x)} = \frac{p(x)}{c_1^2} + \frac{1-p(x)}{c_0^2}. \quad (4.1)$$

### 4.2 Methods to solve the inverse problems

To solve the inverse problem (3.21), gradient-based optimization methods are employed to minimize the misfit between the observed and predicted data. The predicted data is generated by solving the wave equation, and the gradient of the misfit is calculated by solving the adjoint wave equation. The choice of objective function plays a critical role in influencing the quality of inversion results. In this study, we consider two objective functions: the  $L^2$  norm and the

quadratic Wasserstein distance  $W^2$ . Detailed discussions on FWI based on these objective functions can be found in [36, 38, 14]. The  $W^2$  objective function is particularly appealing for several reasons:

1. It facilitates convergence even from a rough initial guess, which is crucial for inverse problems with limited prior knowledge.
2. It promotes smoothness in the recovered model, which aligns well with the smooth nature of the target effective model in our inversion problem.
3. It is demonstrated that  $W^2$  is not very sensitive to oscillations, as highlighted in [38], making it well-suited for applications involving multiscale features.

**Remark 1.** *Given the challenges of directly minimizing the objective function, the multiscale inverse problem formulation (3.21) can be restructured into several alternative formulations to improve the numerical inversion. For example,*

1. *The formulation with model mollification:*

$$\min_{m(x)} \text{dist}(\mathcal{G}_{\text{eff}}(K * m), d_{\text{het}}), \quad (4.2)$$

2. *The formulation with data mollification:*

$$\min_{m(x)} \text{dist}(K * (\mathcal{G}_{\text{eff}}(m)), K * (d_{\text{het}})), \quad (4.3)$$

3. *The formulation with regularization:*

$$\min_{m(x)} \text{dist}(\mathcal{G}_{\text{eff}}(m), d_{\text{het}}) + \alpha \mathcal{R}(m), \quad (4.4)$$

where  $K$  is the mollified kernel,  $\mathcal{R}(m)$  is the regularization term, and  $\alpha$  is the regularization weight. All formulations are motivated by the observation that the effective model and the corresponding measurements exhibit a higher degree of smoothness compared to the heterogeneous model and its associated measurements. The process of mollification plays a crucial role in attenuating oscillatory artifacts present in the inverse problem, thereby enhancing the overall robustness and accuracy of the solution. The regularization term is introduced to prevent overfitting and stabilize the solution by imposing additional constraints on the model parameters. Common choices for the regularization term include Tikhonov regularization, total variation regularization, and sparsity-promoting regularization. Considering the smooth nature of the effective model, the total variation regularization is particularly useful in eliminating the oscillatory artifacts in the solution. We will explore the impact of regularization on the inverse problem in future work.

Next, we will introduce the shot averaging technique to enhance the stability and reliability of the inversion results. The observation that the oscillatory component in  $d_{\text{het}}$  is linked to the sporadic appearance of small-scale reflectors suggests that this effect can be mitigated by averaging over the random medium. To elaborate, we consider a shot averaging technique, which employs a consistent probability pattern  $p(x)$  to generate multiple versions of  $c_\epsilon(x)$ , simulates wave propagation for each of these models and subsequently averages these simulations to derive a new dataset for inversion. More specifically, we generate  $N$  realizations of  $c_\epsilon^{(1)}(x), \dots, c_\epsilon^{(N)}(x)$  from the same probability pattern  $p(x)$ , and solve the wave equation for each realization to obtain the corresponding measurements  $d_{\text{het}}^{(1)}, \dots, d_{\text{het}}^{(N)}$ . The averaged data is then computed as

$$\bar{d}_{\text{het}}(x, t) = \frac{1}{N} \sum_{j=1}^N d_{\text{het}}^{(j)}(x, t). \quad (4.5)$$

Then we replace the synthetic data  $d_{\text{het}}$  with the averaged data  $\bar{d}_{\text{het}}$  in the inverse problem (3.21).

In fact, we aim to approximate the expectation  $\mathbb{E}[u_\epsilon |_{\Gamma \times (0, T)}]$  using a collection of measurements  $d_{\text{het}}^{(1)}, \dots, d_{\text{het}}^{(N)}$ , since  $\mathbb{E}[u_\epsilon |_{\Gamma \times (0, T)}] \rightarrow u |_{\Gamma \times (0, T)}$ . One straightforward approach is to utilize the averaged data  $\bar{d}_{\text{het}}$  to estimate the expectation  $\mathbb{E}[u_\epsilon |_{\Gamma \times (0, T)}]$ , which aligns with our initial idea. However, it is important to note that the averaged shot data  $\bar{d}_{\text{het}}$  might not necessarily serve as the best estimator, i.e., the uniformly minimum variance unbiased estimator, of the expectation  $\mathbb{E}[u_\epsilon |_{\Gamma \times (0, T)}]$ . This discrepancy is tied to the probability distribution of the measurements at a fixed point  $(x, t)$ . Therefore, it becomes imperative to analyze the probability distribution of the measurements and the characteristics of the estimators to ascertain a more optimal estimator.

In practical terms, this technique is akin to collecting repeated measurements over a specific area. While the individual sediment models used in each measurement may vary, they are all governed by the same underlying probability pattern

$p(x)$ . This method effectively averages out the random fluctuations due to the tiny reflectors, thereby enhancing the reliability and stability of the inversion results.

**Remark 2.** *If the probability distribution  $p(x)$  exhibits a low-rank parameterization, one might contemplate bypassing FWI altogether and directly inverting to obtain  $p(x)$ . This alternative could potentially offer a more stable and efficient approach, as it involves a reduction in the dimensionality of the unknown parameter space.*

### 4.3 Determination of sediment concentration

Once we obtain the effective medium model  $\tilde{c}(x)$ , we can determine the sediment distribution  $\tilde{p}(x)$  through direct calculation:

$$\tilde{p}(x) = \frac{\frac{1}{\tilde{c}^2(x)} - \frac{1}{c_0^2}}{\frac{1}{c_1^2} - \frac{1}{c_0^2}}. \quad (4.6)$$

Subsequently, the estimated sediment concentration can be determined by integrating  $\tilde{p}(x)$  over the domain  $D$ . Note that the sediment concentration calculated here is the ratio of the volume of the sediment to the volume of the water, rather than the conventional mass concentration, i.e. the ratio of the mass of the sediment to the volume of the water. However, the mass concentration can be easily calculated by multiplying the volume concentration by the density of the sediment. In the following numerical experiments, we will focus on the volume concentration.

## 5 Numerical results

In this section, we present the numerical results to demonstrate the effectiveness of the proposed model and methods. The numerical experiments are conducted in a two-dimensional domain  $[0, 1 \text{ m}] \times [0, 1 \text{ m}]$ . The domain is discretized into a fine grid with  $5000 \times 5000$  cells and a coarse grid with  $500 \times 500$  cells. The p-wave velocity of the water is  $c_0 = 1500 \text{ m/s}$ , and the p-wave velocity of the sand is  $c_1 = 3000 \text{ m/s}$ . The source (red dots in the following figures) is located along the bottom side of the domain, and the receivers (green diamonds in the following figures) are deployed over the left, top and right sides. The source is a Ricker wavelet with a central frequency of 15 kHz. The time step is  $20 \mu\text{s}$  and  $500 \mu\text{s}$  for the fine mesh and the coarse mesh, respectively. The total simulation time is 1 ms.

For the sediment probability pattern  $p(x)$ , we consider two cases: a Gaussian function and a sediment concentration measured from the real data [8]. The Gaussian function is given by

$$p(x) = p_{\max} \exp\left(-\frac{\|x - x_0\|^2}{2\sigma^2}\right), \quad (5.1)$$

and the concentration measured from the real data is given by

$$p(x) = p_{\max} \left(\frac{x_2}{e^M - x_2(e^M - 1)}\right)^{\lambda G}, \quad G = \frac{1 - e^{-M}}{M\phi}, \quad \phi = \frac{e^M}{e^M - 1} - \frac{1}{M}, \quad (5.2)$$

where  $p_{\max}$  is the maximum sediment concentration,  $x = (x_1, x_2)$  is the spatial variable,  $x_2$  represents the depth,  $M$  and  $\lambda$  are the parameters. The parameters in the following experiments are chosen as  $p_{\max} = 0.002$ ,  $x_0 = (0.5 \text{ m}, 0.5 \text{ m})$ ,  $\sigma = 700$ ,  $M = 1$ , and  $\lambda = 2$ . The sediment concentration is shown in Figure 2. The optimization is performed by the L-BFGS-B algorithm.

### 5.1 Verification of the shot data containing information of sediment concentration

In this section, we first verify that the shot data contain information about the sediment concentration. We compare the shot data in the sediment-laden and sediment-free media. The shot data in the sediment-free media is generated by the homogeneous medium with the p-wave velocity  $c_0 = 1500 \text{ m/s}$ . The shot data in the sediment-laden media is generated by the heterogeneous medium with the sediment concentration  $p(x)$  given by (5.1) and (5.2).

The measurements are shown in Figure 3. Figure 3(a) shows the shot data in the sediment-free media, while Figure 3(b) and Figure 3(c) show the shot data in the sediment-laden media with the sediment concentration given by (5.1) and (5.2), respectively. Figure 3(d) presents the comparison of the shot data in the sediment-laden and sediment-free media.

It can be observed that the shot data in the sediment-laden media exhibit a different pattern compared to the shot data in the sediment-free media, especially the first arrival. The difference in the shot data is due to the presence of the sediment concentration, which affects the wave propagation in the medium. This observation confirms that the shot data contain information about the sediment concentration, which can be utilized to estimate the sediment concentration through the inverse problem.

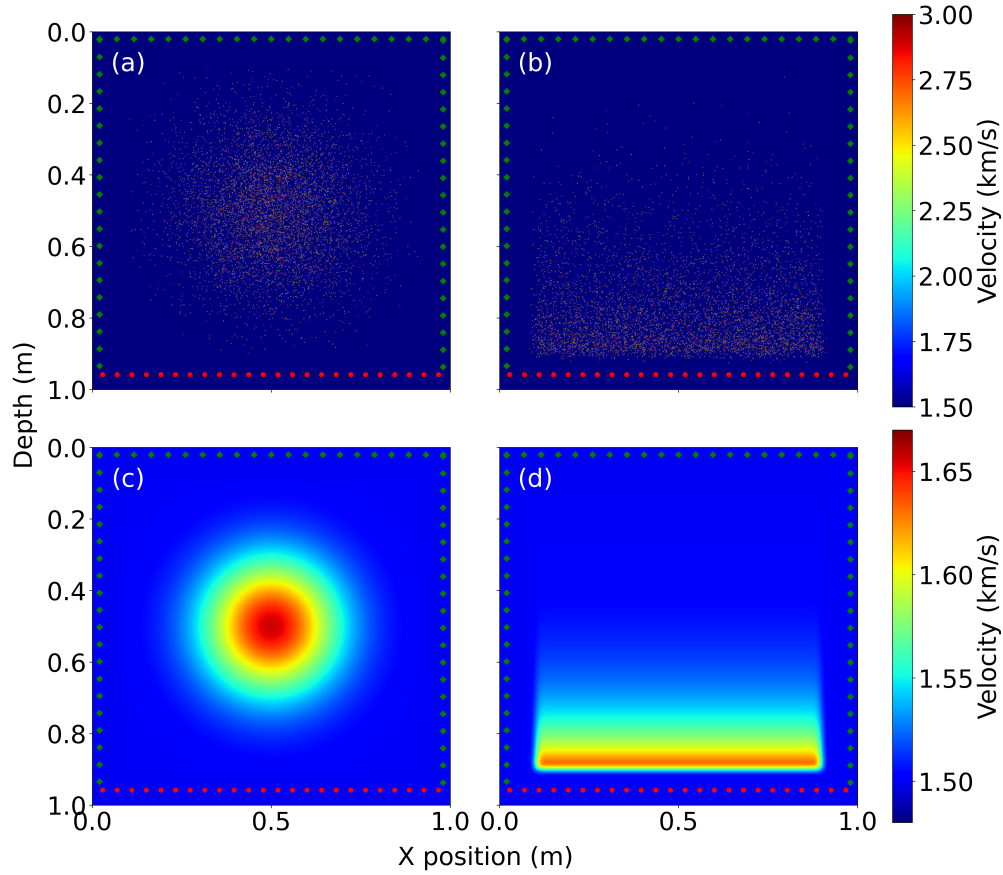


Figure 2: The sediment concentration. (a) Sediment sample  $c_\epsilon(x)$  from Gaussian function. (b) Sediment sample  $c_\epsilon(x)$  from [8]. (c) Effective medium model  $c(x)$  from Gaussian function. (d) Effective medium model  $c(x)$  from [8].

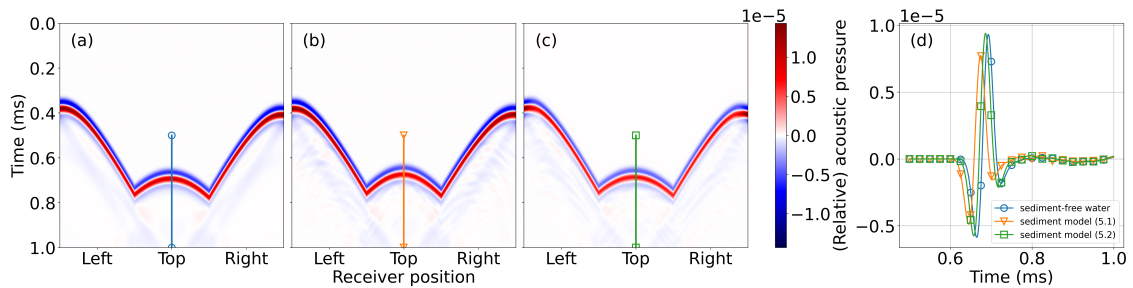


Figure 3: Comparison of shot data in the sediment-laden and sediment-free media. (a) Shot data in the sediment-free media. (b) Shot data in the sediment-laden model (5.1). (c) Shot data in the sediment-laden model (5.2). (d) Comparison of the shot data in the sediment-laden and sediment-free media.

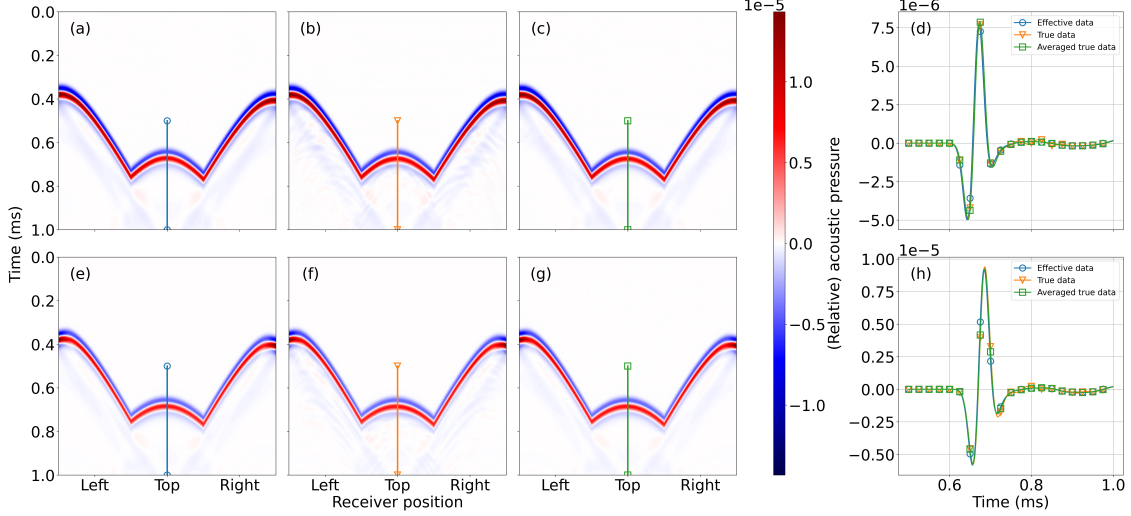


Figure 4: The measurements of the wave field in the heterogeneous medium and the effective medium. The top row shows the results for the Gaussian function, while the bottom row shows the results for the sediment concentration from [8]. (a) Effective data  $d_{\text{eff}}$ . (b) Heterogeneous data  $d_{\text{het}}$ . (c) Averaged heterogeneous data. (d) Comparison for the data from the Gaussian function. (e) Effective data  $d_{\text{eff}}$ . (f) Heterogeneous data  $d_{\text{het}}$ . (g) Averaged heterogeneous data. (h) Comparison for the data from [8].

## 5.2 Data comparison

To demonstrate the approximation of the effective medium model, we first compare the measurements of the wave field in the heterogeneous medium and the effective medium. In this analysis, data  $d_{\text{het}}$  is generated using a heterogeneous medium on a fine grid, while simultaneously  $d_{\text{eff}}$  is produced using the associated effective medium on a coarser grid. The receivers are deployed over the same physical locations (evenly distributed over the left, top and right sides).

The measurements are shown in Figure 4. The top row in Figure 4 shows the results for the Gaussian function, while the bottom row shows the results for the sediment concentration from [8]. The first column shows the effective data  $d_{\text{eff}}$ , the second column shows the heterogeneous data  $d_{\text{het}}$ , and the third column shows the averaged heterogeneous data. The last column shows the comparison of the data in the corresponding colored lines.

It can be observed that the measurements of the wave field in the effective medium are a good approximation of the measurements in the heterogeneous medium except for the multiple scattering parts. In particular, there is only a minor difference between the effective data and the averaged heterogeneous data. The mismatch of the multiple reflection parts is reasonable because the wave field generated by the effective medium model is a zeroth order approximation of the wave field generated by the heterogeneous medium and the minor oscillations align with the high-order terms in the homogenized expansions. For a more accurate approximation, one can consider the higher-order homogenization theory, which can be found in [4, 7, 15, 16]. Overall, the effective medium model captures the direct wave quite well, which is the most important part of the wave field. This result also provides numerical validation of the effectiveness of the effective medium model claimed in Theorem 1.

## 5.3 Inverse crime

Utilizing the effective medium, we generate the synthetic data and perform the inversion with it by FWI. Equivalently, we solve the following minimization problem:

$$\min_{m(x)} \text{dist}(\mathcal{G}_{\text{eff}}(m), d_{\text{eff}}). \quad (5.3)$$

For the inverse crime, all the computations are performed on the coarse mesh, which is optimal for the effective medium.

In the following, we present the true model and inverted models with  $L^2$  and  $W^2$  objective functions in Figure 5. The top row in Figure 5 shows the results for the Gaussian function, while the bottom row shows the results for the sediment concentration from [8]. The left column shows the true effective model, the middle column shows the inverted model with the  $L^2$  objective function, and the right column shows the inverted model with the  $W^2$  objective function.

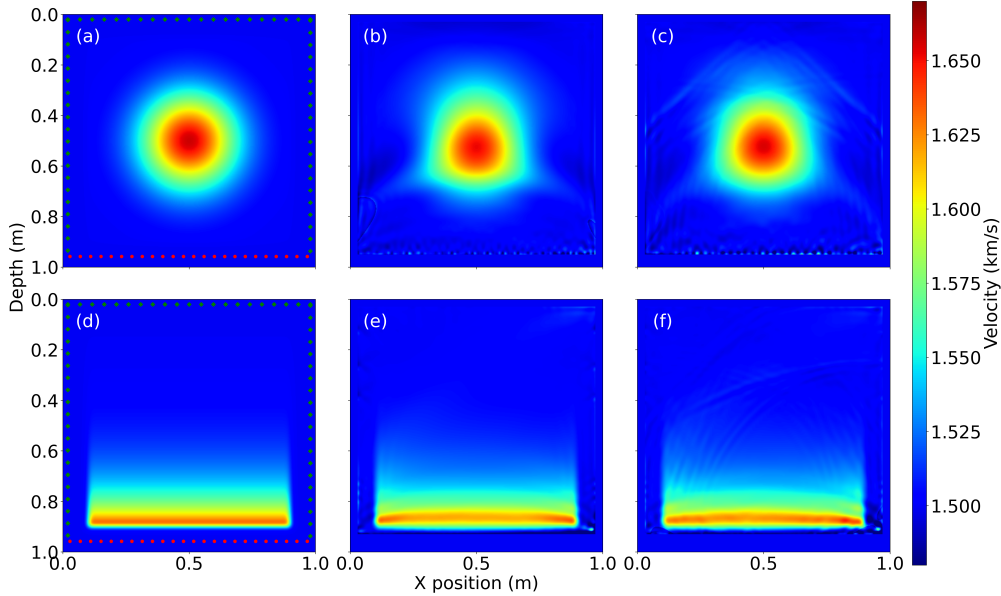


Figure 5: The true model, and inverted models with  $L^2$  and  $W^2$  objective function. The top row shows the results for the Gaussian function, while the bottom row shows the results for the sediment concentration from [8]. (a) True effective model. (b) Inverted model with  $L^2$  objective function. (c) The inverted model with  $W^2$  objective function. (d) True effective model. (e) Inverted model with  $L^2$  objective function. (f) The inverted model with  $W^2$  objective function.

It is noteworthy that both the  $L^2$  and  $W^2$  approaches produce effective reconstructions in this ‘inverse crime’ scenario. The model using the  $W^2$  objective function shows a slightly smaller error. However, the  $L^2$  inverted model yields a smoother result, while the  $W^2$  inverted model exhibits some unexpected oscillatory artifacts near the boundary. Although these artifacts are present, they can be effectively mitigated through post-processing smoothing techniques, as shown in Remark 1. The results with model mollification will be presented in the following subsection.

#### 5.4 Inversion with data generated with heterogeneous medium

In this numerical experiment, we employ the heterogeneous medium to generate the synthetic data and subsequently perform the inversion with it. More precisely, we solve the minimization problem (3.21). For the shot averaging technique, we generate  $N = 50$  realizations of the heterogeneous medium using the same probability pattern  $p(x)$  and solve the wave equation for each realization to obtain the corresponding measurements. The averaged data is then computed according to (4.5).

The true model and the inverted model are shown in Figure 6. The top row in Figure 6 shows the results for the Gaussian function, while the bottom row shows the results for the sediment concentration from [8]. The left column shows the true effective model, while the middle column shows the inverted model without the shot averaging technique. The right column shows the inverted model with the shot averaging technique.

The inverted model without shot averaging exhibits oscillatory artifacts due to the high-frequency nature of the data from the heterogeneous medium, which complicates the inversion process. These oscillations contribute to noise in the inverted model. However, as shown in the right column of Figure 6, the shot averaging technique effectively reduces these oscillatory noises by averaging out random fluctuations, improving the stability and reliability of the inversion. With shot averaging, the inverted model provides a more accurate approximation of the true model, highlighting the technique’s effectiveness in mitigating oscillatory artifacts.

#### 5.5 Inversion with model mollification

According to Remark 1, we consider the inversion with model mollification. The mollified kernel is chosen as the Gaussian function with a standard deviation  $\sigma_{\text{moll}} = 10, 20$  for two cases, respectively.

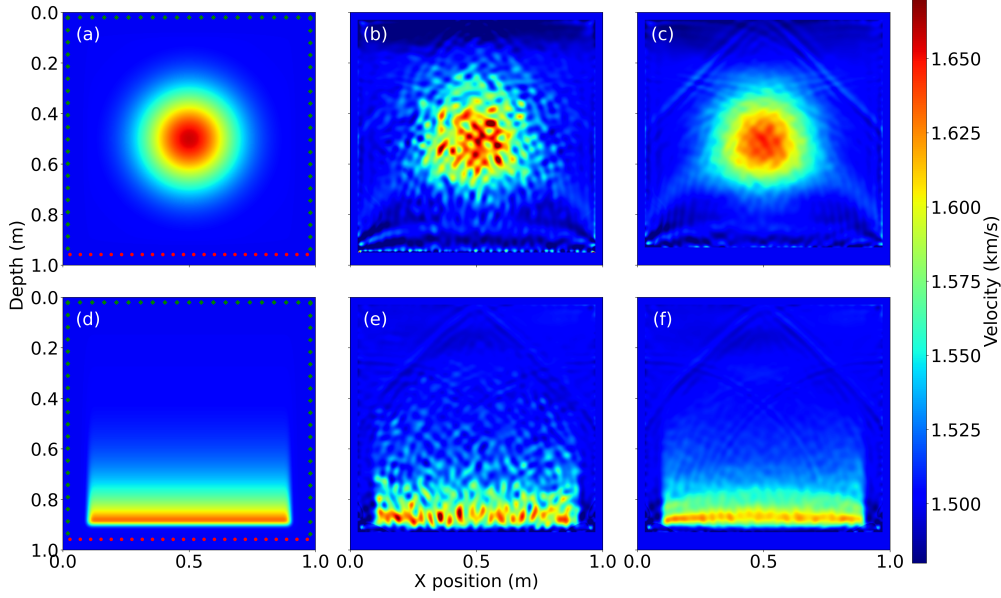


Figure 6: The true model, and inverted models with and without shot averaging technique based on FWI with  $W^2$  objective function. The top row shows the results for the Gaussian function, while the bottom row shows the results for the sediment concentration from [8]. (a) True effective model. (b) Inverted model without shot averaging. (c) The inverted model with shot averaging. (d) True effective model. (e) Inverted model without shot averaging. (f) The inverted model with shot averaging.

The inverted results are shown in Figure 7. The top row shows the results for the Gaussian function, while the bottom row shows the results for the sediment concentration from [8]. The first column shows the true effective model, the second column shows the inverted model with shot averaging, the third column shows the inverted model with model mollification, and the last column shows the inverted model with both shot averaging and model mollification.

One can observe that the oscillatory artifacts in the inverted model are effectively mitigated by the model mollification. The mollified model exhibits a smoother profile, which is more consistent with the true model. Even inversion with only one measurement, the model mollification can still provide a good reconstruction of the true model. This demonstrates the effectiveness of the approach of the model mollification in improving the accuracy of the inversion results. In practical terms, this approach can significantly reduce the computational cost associated with data acquisition, as it eliminates the need for multiple realizations of the heterogeneous medium. Furthermore, the model mollification technique can be easily integrated into existing inversion frameworks, thereby enhancing the precision and reliability of the inversion process. Overall, the combination of the shot averaging technique and model mollification can further enhance the stability and accuracy of the inversion results, as demonstrated in the last column of Figure 7.

## 5.6 Estimation of the sediment concentration

The results obtained from the sediment concentration estimation are presented in Tables 1 and 2. Here we list

1. the true sediment concentrations:
  - (a) the exact sediment concentration calculated from the single sediment sample,
  - (b) the estimated sediment concentration from the probability pattern  $p(x)$  which can be seen as the target value of the inversions,
  - (c) the exact sediment concentration calculated from multiple sediment samples,
2. the measured sediment concentration from the inverted medium  $\tilde{p}(x)$  using four different methods,
3. the relative error between the true value and the measured value.

The reason why we compare the inverted sediment concentrations with three target values is that the true sediment distribution is obtained from a single realization of the probability pattern  $p(x)$ , which is not quite reliable. This sediment concentration would vary from one realization to another, while the estimated sediment concentration from the



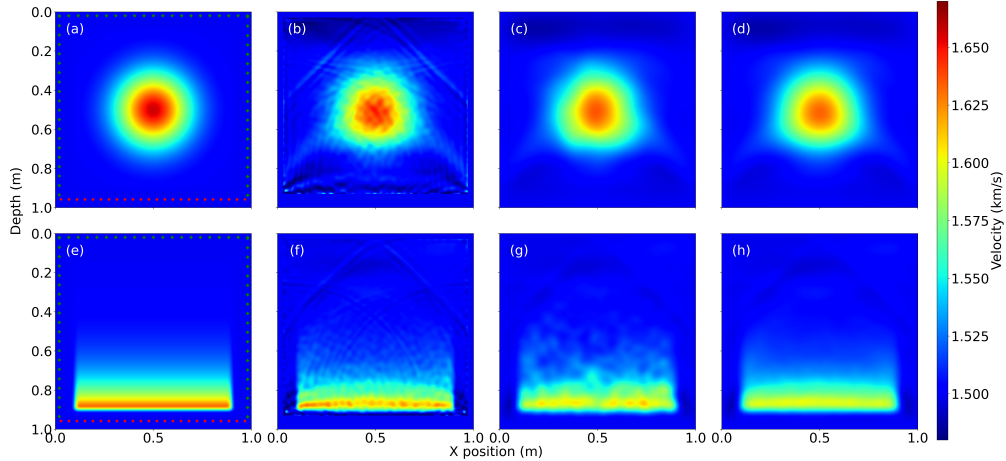


Figure 7: The true model, and inverted models with model mollification based on FWI with  $W^2$  objective function. The top row shows the results for the Gaussian function, while the bottom row shows the results for the sediment concentration from [8]. (a) True effective model. (b) Inverted model with shot averaging. (c) The inverted model with model mollification. (d) The inverted model with shot averaging and model mollification. (e) True effective model. (f) Inverted model with shot averaging. (g) The inverted model with model mollification. (h) The inverted model with shot averaging and model mollification.

probability pattern  $p(x)$  and the average sediment concentration is the mean values of the sediment concentration of all the realizations, which are more reliable. Hence, the comparison with the estimated values from the probability pattern  $p(x)$  and the exact values calculated from the multiple realizations can provide a more comprehensive evaluation of the inversion results.

The results demonstrate a strong agreement between the estimated and actual sediment concentrations, highlighting the accuracy of the estimation process. Furthermore, the application of the model mollification method significantly improves the accuracy of the sediment concentration estimates, as reflected in the reduced relative errors. However, it is important to note that the relative errors cannot be completely eliminated due to the zeroth order approximation inherent in the effective medium model.

Moreover, it is important to note that the shot averaging technique would not necessarily decrease the relative error of the estimated sediment concentration. This is because there are still minor oscillations in the averaged data, which leads to the limited improvement of the inversion results. Hence, it could not improve the inversion results in the direct way as the model mollification method, especially when the domain of sediment concentration is small, such as the model from [8]. Nevertheless, it is still beneficial to apply the shot averaging technique for the case of large domain of sediment concentration, such as the Gaussian model, as it can reduce the error of the estimated sediment concentration.

Another observation is that the combination of the shot averaging technique and the model mollification method does not necessarily provide the best inversion results. We speculate that the combination of these two techniques may lead to over-smoothing of the inverted model, which could potentially result in the loss of some high-frequency information and the local peaks in the inverted model. This could explain the relatively higher relative errors of the estimated sediment concentration in the last row of Tables 1 and 2.

Overall, the results demonstrate the outstanding performance of the proposed approach in estimating the sediment concentration, thereby highlighting its potential for practical applications in the field of sediment concentration estimation.

## 6 Conclusion

In this study, we have introduced a novel model that is based on the multiscale inverse problem formulation for accurately measuring sediment concentration. Initially, we characterized sediment concentration as an inhomogeneous random field and addressed the measurement challenge as a multiscale inverse problem. Leveraging stochastic homogenization theory, we derived an effective medium model and developed numerical techniques tailored to the multiscale

Table 1: The relative errors of estimated sediment concentration of Gaussian model. (–: without improvement method)

Improvement method	Inverted value	True values		
		Exact (single)	Estimated from $p(x)$	Exact (multiple)
		0.0277	0.0294	0.0279
–	0.0252	8.7918 %	14.3122 %	9.7560 %
shot averaging	0.0260	5.9385 %	11.6316 %	6.9329 %
model mollification	0.0267	3.5592 %	9.3964 %	4.5788 %
shot averaging + model mollification	0.0263	4.9898 %	10.7404 %	5.9942 %

Table 2: The relative errors of estimated sediment concentration of model from [8]. (–: without improvement method)

Improvement method	Inverted value	True values		
		Exact (single)	Estimated from $p(x)$	Exact (multiple)
		0.0251	0.0268	0.0255
–	0.0233	7.0658 %	13.1448 %	8.4799 %
shot averaging	0.0230	8.3619 %	14.3562 %	9.7563 %
model mollification	0.0240	4.2620 %	10.5245 %	5.7188 %
shot averaging + model mollification	0.0231	7.7666 %	13.7998 %	9.1700 %

nature of the problem. Our numerical experiments demonstrated the efficacy of the proposed model and methodologies, producing estimates of sediment concentration that closely align with true values.

Moving forward, our research will concentrate on the following aspects for enhancement:

1. It is important to acknowledge that the operator  $\mathcal{G}_{\text{eff}}$  offers only a zeroth order approximation of the operator  $\mathcal{G}_{\text{het}}^\epsilon$ . To achieve improved approximations on a larger scale, exploring higher-order homogenization theories is recommended.
2. A more comprehensive analysis of the convergence of  $u_\epsilon(x, t)$  to  $u(x, t)$  as  $\epsilon \rightarrow 0$  is imperative for a deeper understanding of the model's behavior, particularly in the context of more general stochastic media beyond the heterogeneous Poisson point process examined in this study.

By addressing these areas, we aim to further refine our model and methodologies, ultimately advancing the accuracy and applicability of sediment concentration measurements.

## References

- [1] Assyr Abdulle and Andrea Di Blasio. A bayesian numerical homogenization method for elliptic multiscale inverse problems. *SIAM/ASA Journal on Uncertainty Quantification*, 8(1):414–450, January 2020.
- [2] D. S. Bhargava and Dejene W. Mariam. Light penetration depth, turbidity and reflectance related relationship and models. *ISPRS Journal of Photogrammetry and Remote Sensing*, 46(4):217–230, August 1991.
- [3] K. P. Black and M. A. Rosenberg. Suspended sand measurements in a turbulent environment: Field comparison of optical and pump sampling techniques. *Coastal Engineering*, 24(1):137–150, November 1994.
- [4] Y. Capdeville and J.-J. Marigo. Second order homogenization of the elastic wave equation for non-periodic layered media. *Geophysical Journal International*, 170(2):823–838, 2007.
- [5] Yann Capdeville, Laurent Guillot, and Jean-Jacques Marigo. 1-D non-periodic homogenization for the seismic wave equation. *Geophysical Journal International*, 181(2):897–910, May 2010.
- [6] Yann Capdeville, Laurent Guillot, and Jean-Jacques Marigo. 2-D non-periodic homogenization to upscale elastic media for P–SV waves. *Geophysical Journal International*, 182(2):903–922, August 2010.
- [7] W. Chen and J. Fish. A dispersive model for wave propagation in periodic heterogeneous media based on homogenization with multiple spatial and temporal scales. *Journal of Applied Mechanics*, 68(2):153–161, August 2000.

- [8] Chao-Lin Chiu, Weixia Jin, and Yen-Chang Chen. Mathematical models of distribution of sediment concentration. *Journal of Hydraulic Engineering*, 126(1):16–23, January 2000.
- [9] V. K. Choubey. The effect of properties of sediment type on the relationship between suspended sediment concentration and radiance. *Hydrological Sciences Journal*, 39(5):459–470, October 1994.
- [10] N. J. Clifford, K. S. Richards, R. A. Brown, and S. N. Lane. Laboratory and field assessment of an infrared turbidity probe and its response to particle size and variation in suspended sediment concentration. *Hydrological Sciences Journal*, 40(6):771–791, December 1995.
- [11] A. M. Crawford and Alex E. Hay. Determining suspended sand size and concentration from multifrequency acoustic backscatter. *The Journal of the Acoustical Society of America*, 94(6):3312–3324, December 1993.
- [12] Weinan E and Bjorn Engquist. The Heterogeneous Multiscale Methods. *Communications in Mathematical Sciences*, 1(1):87–132, March 2003.
- [13] Ş. Elçi, R. Aydin, and P. A. Work. Estimation of suspended sediment concentration in rivers using acoustic methods. *Environmental Monitoring and Assessment*, 159(1-4), December 2009.
- [14] Björn Engquist and Yunan Yang. Optimal transport based seismic inversion: Beyond cycle skipping. *Communications on Pure and Applied Mathematics*, 75(10):2201–2244, 2022.
- [15] Jacob Fish and Wen Chen. Higher-order homogenization of initial/boundary-value problem. *Journal of Engineering Mechanics*, 127(12):1223–1230, December 2001.
- [16] Jacob Fish, Wen Chen, and Gakuji Nagai. Non-local dispersive model for wave propagation in heterogeneous media: One-dimensional case. *International Journal for Numerical Methods in Engineering*, 54(3):331–346, 2002.
- [17] Christina Frederick and Björn Engquist. Numerical methods for multiscale inverse problems. *Comm. Math. Sci.*, 15(2):305–328, 2017.
- [18] J Gao and S. M. O’leary. The role of spatial resolution in quantifying SSC from airborne remotely sensed data. *Photogrammetric Engineering & Remote Sensing*, 63(3):267–271, 1997.
- [19] J. R. Gray, G. D. Glysson, and D. S. Mueller. Comparability and accuracy of fluvial-sediment data - A view from the U.S. Geological Survey. In *Hydraulic Measurements and Experimental Methods 2002*, pages 919–924, 2002.
- [20] Malcolm O. Green and John D. Boon. The measurement of constituent concentrations in nonhomogeneous sediment suspensions using optical backscatter sensors. *Marine Geology*, 110(1):73–81, February 1993.
- [21] Laurent Guillot, Yann Capdeville, and Jean-Jacques Marigo. 2-D non-periodic homogenization of the elastic wave equation: SH case. *Geophysical Journal International*, 182(3):1438–1454, September 2010.
- [22] H. K. Ha, W. Y. Hsu, J. P. Y. Maa, Y. Y. Shao, and C. W. Holland. Using ADV backscatter strength for measuring suspended cohesive sediment concentration. *Continental Shelf Research*, 29(10):1310–1316, May 2009.
- [23] D.M. Hanes, C.E. Vincent, D.A. Huntley, and T.L. Clarke. Acoustic measurements of suspended sand concentration in the C2S2 experiment at Stanhope Lane, Prince Edward Island. *Marine Geology*, 81(1-4):185–196, June 1988.
- [24] Juha Heinonen. *Lectures on Analysis on Metric Spaces*. Universitext. Springer, New York, 2001.
- [25] S. A. Hosseini, A. Shamsai, and B. Ataie-Ashtiani. Synchronous measurements of the velocity and concentration in low density turbidity currents using an Acoustic Doppler Velocimeter. *Flow Measurement and Instrumentation*, 17(1):59–68, March 2006.
- [26] Wenjia Jing and Olivier Pinaud. A backscattering model based on corrector theory of homogenization for the random Helmholtz equation. *Discrete & Continuous Dynamical Systems - B*, 24(10):5377–5407, 2019.
- [27] J. F. C. Kingman. *Poisson Processes*. Number 3 in Oxford Studies in Probability. Clarendon Press, Oxford, 1993.
- [28] Patrick Lailly. The seismic inverse problem as a sequence of before stack migrations. In *Conference on Inverse Scattering: Theory and Application*, pages 206–220, Philadelphia, Pa, 1983.
- [29] Keith A Ludwig and Daniel M Hanes. A laboratory evaluation of optical backscatterance suspended solids sensors exposed to sand-mud mixtures. *Marine Geology*, 94(1):173–179, July 1990.
- [30] Ramazan Meral. A study on the estimating of sediment concentration with turbidity and acoustic backscatter signal for different sediment sizes. *Hydrology Research*, 47(2):305–311, November 2015.
- [31] James Nolen and George Papanicolaou. Fine scale uncertainty in parameter estimation for elliptic equations. *Inverse Problems*, 25(11):115021, November 2009.

- [32] James Nolen, Grigorios A. Pavliotis, and Andrew M. Stuart. Multiscale Modelling and Inverse Problems. In Ivan G. Graham, Thomas Y. Hou, Omar Lakkis, and Robert Scheichl, editors, *Numerical Analysis of Multiscale Problems*, Lecture Notes in Computational Science and Engineering, pages 1–34. Springer, Berlin, Heidelberg, 2012.
- [33] E. M. M. Novo, J. D. Hansom, and P. J. Curran. The effect of sediment type on the relationship between reflectance and suspended sediment concentration. *International Journal of Remote Sensing*, 10(7):1283–1289, July 1989.
- [34] E. M. M. Novo, J. D. Hansom, and P. J. Curran. The effect of viewing geometry and wavelength on the relationship between reflectance and suspended sediment concentration. *International Journal of Remote Sensing*, 10(8):1357–1372, August 1989.
- [35] Francisco Pedocchi and Marcelo H. García. Acoustic measurement of suspended sediment concentration profiles in an oscillatory boundary layer. *Continental Shelf Research*, 46:87–95, September 2012.
- [36] R.-E. Plessix. A review of the adjoint-state method for computing the gradient of a functional with geophysical applications. *Geophysical Journal International*, 167(2):495–503, November 2006.
- [37] Flóra Pomázi and Sándor Baranya. Acoustic based assessment of cross-sectional concentration inhomogeneity at a suspended sediment monitoring station in a large river. *Acta Geophysica*, 70(5):2361–2377, October 2022.
- [38] Lingyun Qiu. Analysis of seismic inversion with optimal transportation and softplus encoding. *Inverse Problems*, 37(9):095004, August 2021.
- [39] Mehrdad Salehi and Kyle Strom. Using velocimeter signal to noise ratio as a surrogate measure of suspended mud concentration. *Continental Shelf Research*, 31(9):1020–1032, June 2011.
- [40] D. H. Schoellhamer and S. A. Wright. Continuous monitoring of suspended sediment in rivers by use of optical backscatterance sensors. In *Erosion and Sediment Transport Measurement in Rivers : Technological and Methodological Advances*, pages 28–36, 2002.
- [41] Albert Tarantola. Inversion of seismic reflection data in the acoustic approximation. *Geophysics*, 49(8):1259–1266, August 1984.
- [42] Peter D. Thorne and Daniel M. Hanes. A review of acoustic measurement of small-scale sediment processes. *Continental Shelf Research*, 22(4):603–632, March 2002.
- [43] Peter D. Thorne and Peter J. Hardcastle. Acoustic measurements of suspended sediments in turbulent currents and comparison with *in-situ* samples. *The Journal of the Acoustical Society of America*, 101(5):2603–2614, May 1997.
- [44] Eric D. Thosteson and Daniel M. Hanes. A simplified method for determining sediment size and concentration from multiple frequency acoustic backscatter measurements. *The Journal of the Acoustical Society of America*, 104(2):820–830, August 1998.
- [45] David J. Topping and Scott A. Wright. Long-term continuous acoustical suspended-sediment measurements in rivers - Theory, application, bias, and error. Technical Report 1823, U.S. Geological Survey, 2016.
- [46] D. G. Wren, B. D. Barkdoll, R. A. Kuhnle, and R. W. Darrow. Field techniques for suspended-sediment measurement. *Journal of Hydraulic Engineering*, 126(2):97–104, February 2000.
- [47] J. P. Xu. Converting near-bottom OBS measurements into suspended sediment concentrations. *Geo-Marine Letters*, 17(2):154–161, April 1997.